

## Article

# Combined DFT-D3 Computational and Experimental Studies on g-C<sub>3</sub>N<sub>4</sub>: New Insight into Structure, Optical, and Vibrational Properties

Paolo Negro , Federico Cesano , Silvia Casassa  and Domenica Scarano 

Department of Chemistry and NIS (Nanostructured Interfaces and Surfaces) Interdepartmental Centre, University of Torino & INSTM-UdR Torino, Via P. Giuria 7, 10125 Torino, Italy; federico.cesano@unito.it (F.C.); silvia.casassa@unito.it (S.C.)

\* Correspondence: pa.negro@unito.it (P.N.); domenica.scarano@unito.it (D.S.); Tel.: +39-011-6707834 (D.S.)

**Abstract:** Graphitic carbon nitride (g-C<sub>3</sub>N<sub>4</sub>) has emerged as one of the most promising solar-light-activated polymeric metal-free semiconductor photocatalysts due to its thermal physicochemical stability but also its characteristics of environmentally friendly and sustainable material. Despite the challenging properties of g-C<sub>3</sub>N<sub>4</sub>, its photocatalytic performance is still limited by the low surface area, together with the fast charge recombination phenomena. Hence, many efforts have been focused on overcoming these drawbacks by controlling and improving the synthesis methods. With regard to this, many structures including strands of linearly condensed melamine monomers, which are interconnected by hydrogen bonds, or highly condensed systems, have been proposed. Nevertheless, complete and consistent knowledge of the pristine material has not yet been achieved. Thus, to shed light on the nature of polymerised carbon nitride structures, which are obtained from the well-known direct heating of melamine under mild conditions, we combined the results obtained from XRD analysis, SEM and AFM microscopies, and UV-visible and FTIR spectroscopies with the data from the Density Functional Theory method (DFT). An indirect band gap and the vibrational peaks have been calculated without uncertainty, thus highlighting a mixture of highly condensed g-C<sub>3</sub>N<sub>4</sub> domains embedded in a less condensed “melon-like” framework.

**Keywords:** graphitic carbon nitrides; melon polymorph structure; DFT-D3 computation; structure and morphological properties; optical properties; vibrational properties



**Citation:** Negro, P.; Cesano, F.; Casassa, S.; Scarano, D. Combined DFT-D3 Computational and Experimental Studies on g-C<sub>3</sub>N<sub>4</sub>: New Insight into Structure, Optical, and Vibrational Properties. *Materials* **2023**, *16*, 3644. <https://doi.org/10.3390/ma16103644>

Academic Editors: Alina Pruna and Alexander N. Obraztsov

Received: 24 March 2023

Revised: 3 May 2023

Accepted: 6 May 2023

Published: 10 May 2023



**Copyright:** © 2023 by the authors. Licensee MDPI, Basel, Switzerland. This article is an open access article distributed under the terms and conditions of the Creative Commons Attribution (CC BY) license (<https://creativecommons.org/licenses/by/4.0/>).

## 1. Introduction

The prospect of developing inexpensive, energy-efficient, green, and sustainable industrial processes has attracted extensive interest in the scientific and industrial communities. For this reason, in the past few years, among the carbon-based materials, g-C<sub>3</sub>N<sub>4</sub>, a polymeric metal-free semiconductor photocatalyst with 2D graphene-like structure, has received massive attention [1–7]. Due to its exceptional properties, including easy preparation methods from economical raw materials (i.e., earth-abundant carbon- and nitrogen-based materials), high thermal and chemical stabilities, non-toxicity, tunable band gap, and visible light absorption, it turns out that widespread applications, such as the removal of toxic metal ions, degradation of dye pollutants, selective organic transformation to fine chemicals, and photocatalysis for hydrolytic hydrogen production, have been developed [8–12]. Moreover, it can be used in additional fields such as metal-free organic syntheses [13–20], solar-light-driven photo-redox catalysis, photocatalytic water splitting, photoelectric conversion, and fuel cells [9,12].

It is well known that g-C<sub>3</sub>N<sub>4</sub> is a n-type semiconductor, the framework of which is formed of  $\pi$ -conjugated N-bridged aromatic poly tri-s-triazine units (heptazine rings) forming layers with strong C-N covalent bonds. Namely, it was found that the 2D lattice consists of a periodic arrangement of nitrogen-linked heptazine units, in which each nitrogen connects two or three heptazine rings, thus giving rise to a variety of structural

motifs with different levels of condensation, ranging from partially to fully polymerised structures [21,22]. The  $\pi$ -conjugated  $sp^2$  hybridised structure is also responsible for the visible light absorption at about 460 nm, which explains the typical pale yellow colour [23].

Regarding the thermal properties,  $g\text{-C}_3\text{N}_4$  is highly stable up to 600 °C, with C-N fragmentation reactions occurring at higher temperature, while concerning the chemical stability, the van der Waals interactions among layers render it non-reactive to many conventional solvents [13].

However, some drawbacks must be mentioned, including the low specific surface area, the chemical inertness itself, the poor charge carrier mobility, and the high exciton recombination rates. Nevertheless, since  $g\text{-C}_3\text{N}_4$  has been considered a promising/challenging material in many fields [24–26], to overcome the aforementioned drawbacks, and also to improve its already existing properties,  $g\text{-C}_3\text{N}_4$  has been combined often with metals or other semiconductors to form heterojunctions or composites with innovative architectures, aiming at enhancing the charge carrier rates, the surface properties, the surface area, etc. [27]. Concerning the innovative architectures, low dimensional carbon nitride nanostructures, i.e., 1D nanowires, nanotubes, or nanorods, as well as 2D nanosheets, show improved charge transfer ability compared to the bulk structures. Furthermore, porous 3D nanospheres provide an increased specific surface area, thus also improving adsorption ability and, ultimately, the photocatalytic performance [21,28]. In this respect, detailed investigations on the surface properties of carbon nitride structures with different polymerisation degrees have been carried out to understand the role of terminal amino groups and (C=N–C) neighbouring triazine nitrogen units in catalytic reactions as potential active sites to form heterostructures [29].

It is known that, due to the commonly used synthesis methods (thermal polycondensation in air), high crystalline  $g\text{-C}_3\text{N}_4$  structures are difficult to obtain [3]. This means that the peculiar properties of  $g\text{-C}_3\text{N}_4$  itself depend strongly on the experimental conditions, i.e., on the different precursors that are used during the synthesis, on the reaction rates, and/or temperatures, thus affecting the local structure, the stacking order, and the formation of defective situations, which play a significant role in modifying the band structures [5,23].

On this matter, several computation models have been proposed and compared with the experimental data by changing the stacking order and the inter-layer and inner-layer distances between heptazine chains, together with, in some cases, ring-opening reactions, which give rise to nitrogen defects, thus increasing the complexity of the models [6,30–33]. Despite the many efforts focused either on experimental (i.e., neutron and X-ray diffraction patterns) and on computational approaches [3], which predict amazing properties and applications, the complex structure of the polymeric carbon nitride systems is still poorly understood, being, therefore, also a matter of a controversial debate [14,34,35].

Along this theme, our aim is to give some insights into the more suitable carbon nitride model with a stable configuration, which is able to describe properly the experimental results obtained from X-ray diffraction patterns, UV-visible, and FTIR spectra. Therefore, two structures with two different degrees of condensation of  $g\text{-C}_3\text{N}_4$  systems have been investigated and characterised at the Density Functional Theory level (DFT) by means of the periodic simulation code CRYSTAL [36]. Indeed, interestingly, a realistic model that is able to explain the experimentally measured properties is based on the coexistence of different structural motifs. As previously stated, it is challenging for the adopted approach to shed light on the electronic structure of both partially (melon-like) and fully ( $g\text{-C}_3\text{N}_4$ ) polymerised systems as such, with the aim of developing more complex heterostructures such as homo–heterojunctions, which could enable a more effective light absorption with the consequent use in visible-light-responsive photocatalysis.

With regard to this, it is well known that DFT calculations can also provide a description of the valence and conduction bands in terms of atomic orbitals, which potentially play a relevant role as oxidation and reduction sites in photocatalysis [2].

## 2. Computational Set Up

Throughout this work, we apply DFT as implemented in CRYSTAL17 [36], a periodic quantum-mechanical code based on the description of the crystalline wave function as a linear combination of localised Gaussian-type atomic orbitals.

A 6-21G basis set plus polarisation functions (3-1G for hydrogen atoms), which is used extensively for solid-state system calculation, was adopted for C and N atoms and will be referred to in the following sections as 621pol [37]. Functionals with different percentage of Hartree–Fock (HF) exchange have been explored, including pure Perdew–Burke–Ernzerhof functional (PBE) [38], PBE0 (25% of exact change) [39,40], and HSE06 [41] (Table S1). The calculations were finally performed at the PBE/621pol level. Moreover, since the van der Waals interactions play a fundamental role in establishing these materials, the PBE was enriched with the D3 a-posteriori empirical correction proposed by Grimme [42] to account for the London dispersion forces (PBE-D3).

The DFT exchange–correlation contribution was evaluated via numerical integration over the unit cell volume by using a pruned grid with 99 radial and 1454 angular points. Integration over the reciprocal space was carried out by using Pack–Monkhorst meshes of  $4 \times 4 \times 4$ . The Coulomb and exchange series, which were summed in direct space, were truncated by using overlap criteria thresholds of [7, 7, 7, 12, 24]. Convergence for the self-consistent field algorithm was achieved up to a threshold of  $10^{-9}$  Hartree on the total energy, per unit cell [43].

Geometry optimisation was performed by using analytical gradients with respect to atomic co-ordinates and unit cell parameters, within a quasi-Newtonian scheme combined with Broyden–Fletcher–Goldfarb–Shanno Hessian updating [44,45]. The default convergence criteria were adopted for both gradient components and nuclear displacements.

A full set of vibrational frequencies in  $k = \Gamma$  was obtained within the harmonic approximation by diagonalising the mass-weighted Hessian matrix. This matrix was built by numerically differencing the analytical gradient with respect to atomic cartesian co-ordinates [46,47].

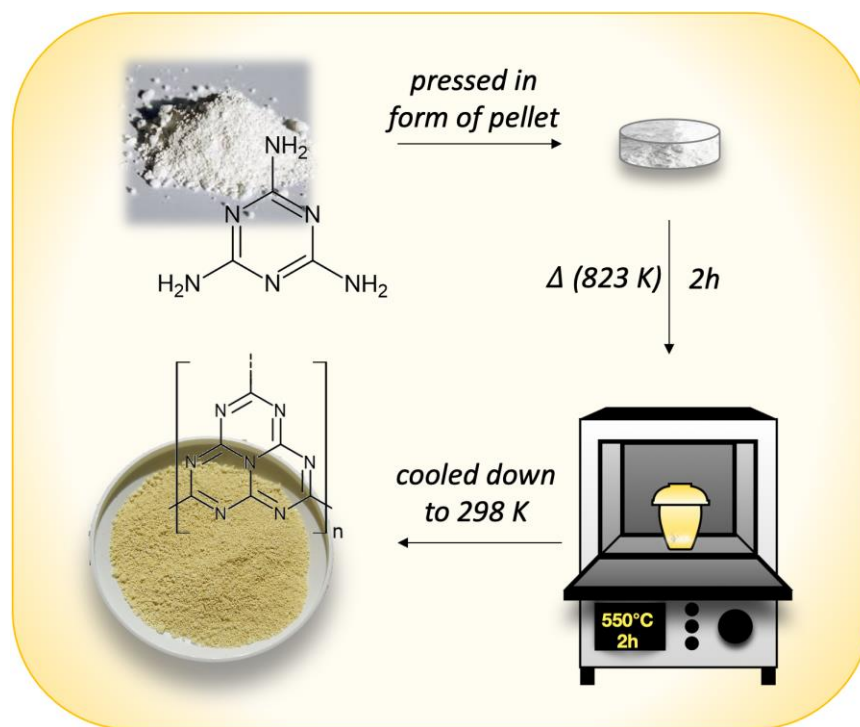
The topological analysis of electron density, which allows an accurate mapping of bonds and atoms, was carried out by means of the TOPOND [48] program, which was recently incorporated in the CRYSTAL [48–50] code. The topological properties of the critical points of the bonds were analysed according to Bader’s theory of atoms in molecules and crystals (QTAMAC) [51] to acquire information on the number and type of interactions.

## 3. Materials and Methods

Graphitic carbon nitride ( $g\text{-C}_3\text{N}_4$ ) was prepared by heating 2 g of melamine powder (Sigma-Aldrich, Burlington, MO, USA, Melamine 99% M2659) inside a muffle (Nabertherm B400). In more detail, to avoid the melamine leak during the precursor sublimation, the powder was pressed into the form of a pellet and introduced in a ceramic crucible, which was closed with a ceramic lid (even if not-hermetically). The sample was heated up to a temperature of 823 K with a heating rate of 1 K per minute and kept for 2 h at the same temperature. Then the sample was slowly cooled down to room temperature and weighed (resulting in about 48% of the initial mass) (see Scheme 1).

From the photograph in Scheme 1, it appears that the obtained material on the white sample holder shows a yellowish colour, which makes it possible to predict the energy value of the absorption edge in the UV-Vis diffuse reflectance spectra (vide infra).

The X-ray diffraction patterns were obtained by using a PANalytical PW3050/60 X’Pert PRO MPD X-ray diffractometer with a Cu radiation ( $K\alpha = 1.54060 \text{ \AA}$ ) and a Ni filter in Bragg–Brentano configuration, which was equipped with a X’Celerator detector. The diffractograms were acquired in the  $5^\circ \leq 2\theta \leq 80^\circ$  interval with an acquisition step of  $0.01^\circ$ .



**Scheme 1.** Main steps of g-C<sub>3</sub>N<sub>4</sub> synthesis.

N<sub>2</sub> adsorption–desorption experiments were carried out at 77 K by a Micromeritics ASAP 2020 instrument (Micromeritics, Norcross, GA, USA) to determine the Brunauer–Emmett–Teller (BET) surface area. The surface area of the samples was determined after outgassing at 423 K, overnight.

Scanning Electron Microscopy (SEM) analyses were carried out by using a ZEISS EVO 50 XVP microscope with a LaB<sub>6</sub> source. Before performing the analysis, the insulating samples were covered with a gold layer of about 15 nm in thickness to avoid any charging effect (Bal-tec SCD050 sputter coater).

Atomic Force Microscopy measurements were carried out in the Intermittent-Contact (IC) mode by using a modified Nanosurf Easyscan2 AFM instrument, which was equipped with a 10 μm scan-head, inside a shielded and acoustically insulated enclosure on a high-performance anti-vibration platform.

The optical properties were investigated in the 190–2500 nm wavelength range by means of a Cary 5000 UV-vis-NIR spectrophotometer, which was equipped with a diffuse reflectance sphere in the diffuse reflectance (DR) mode. The sample was diluted in PTFE powder (2% by weight).

FTIR spectra were acquired in transmission mode by means of a Bruker VECTOR22 spectrometer that was equipped with a cryogenic MCT detector with 2 cm<sup>−1</sup> resolution. Due to the high absorbance of the sample in the IR spectrum, the material was diluted in KBr (2% by weight). Each sample was pressed in the form of self-supporting pellets and then analysed under vacuum at 298 K.

## 4. Results and Discussion

### 4.1. Crystal Structure by XRD Analysis and Modelling

#### 4.1.1. Experimental XRD Analysis

From the X-ray diffraction pattern of our specimen (Figure 1, black line), two main peaks at approximately 13.04° and 27.6° are both assigned to layered g-C<sub>3</sub>N<sub>4</sub> systems, in agreement with the literature data [7,52–56]. In particular, the feature at 27.6° (002), which is typical of the layered structure, is due to the inter-layer π–π stacking with a distance d(002) = 3.218 v.

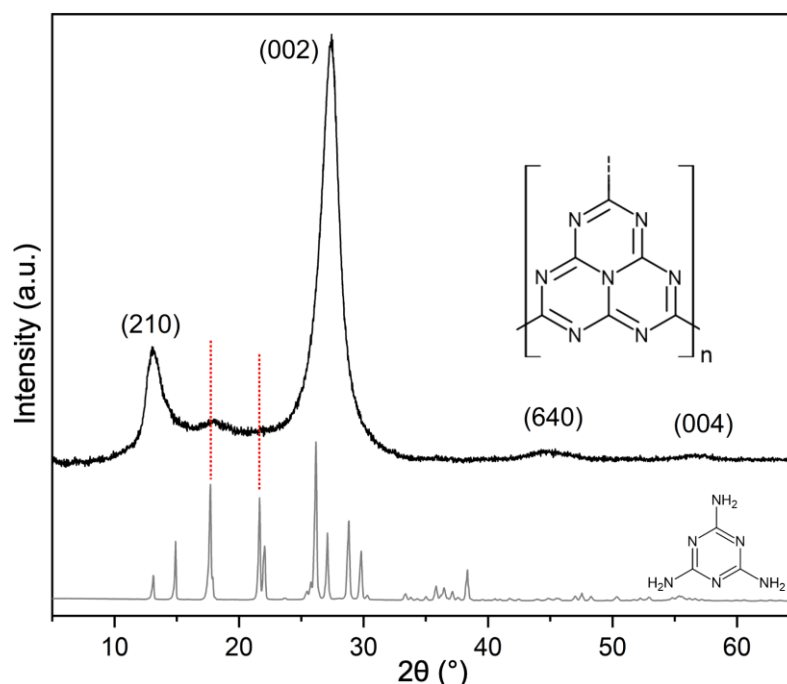


**Figure 1.** XRD patterns of the synthesised sample (black line) and of melamine (grey line). Red dotted lines highlight the presence of weak melamine features in the diffraction pattern of our sample.

The feature at  $2\theta = 13.04^\circ$  represents the in-plane packing of heptazine units and could be assigned either to the (210) diffraction planes of an orthorhombic unit cell [7] or to the (100) diffraction planes of a hexagonal unit cell [52–55].

For the sake of comparison, the XRD pattern of pure melamine powder has been shown (Figure 1, grey line). Due to the presence of broad and weak reflections at approximately  $2\theta = 17.7^\circ$  and  $2\theta = 21.9^\circ$  on the pattern of our specimen (red dotted lines), which are typical of melamine, it can be reasonably hypothesised that a network of hydrogen-bonded melamine/triazine units is present inside the heptazine framework.

From Scherrer's equation  $D = k\lambda/\beta\cos\theta$ , where  $\lambda$  is the X-ray wavelength,  $\beta$  is the FWHM of the diffraction line corrected by the instrumental broadening,  $\theta$  is the diffraction angle, and  $K$  is Scherrer's constant or shape constant, which has been assumed to be 0.9, in agreement with Alizadeh et al. [57], the mean crystallite thickness of the particles has been calculated. In particular, from the (002) XRD peak (i.e.,  $2\theta = 27.6^\circ$ ), the estimated dimension of the scattering domains is about 48 nm, in agreement with the BET surface area (about  $9 \text{ m}^2/\text{g}$ ).

#### 4.1.2. Modelling the Crystal Structure

In this work, among the many structures proposed for carbon nitride polymerised structures, including  $g\text{-C}_3\text{N}_4$ , which was subjected to extensive and controversial discussions [1–7], we adopted the model proposed by Fina et al. based on their XRD and neutron diffraction analyses [7], which are reported for the sake of comparison in the a and c panels of Figure 2.

After a complete geometry optimisation at the PBE-D3/621pol level, the system produced results as in the b and d panels of Figure 2.

The peculiar intra-layer melon-like structure is retained, but the interplanar distance decreases, and a remarkable zig-zag layer deformation occurs. The data, which is reported in Table 1, confirm the aforementioned structural relaxation, which causes a contraction of the  $a$ , along the  $z$  direction, together with a slight increase in the  $b$  and  $c$  parameters with respect to the experimental values. As a result, a decrease in the total volume of the unit cell of about 5% is obtained.

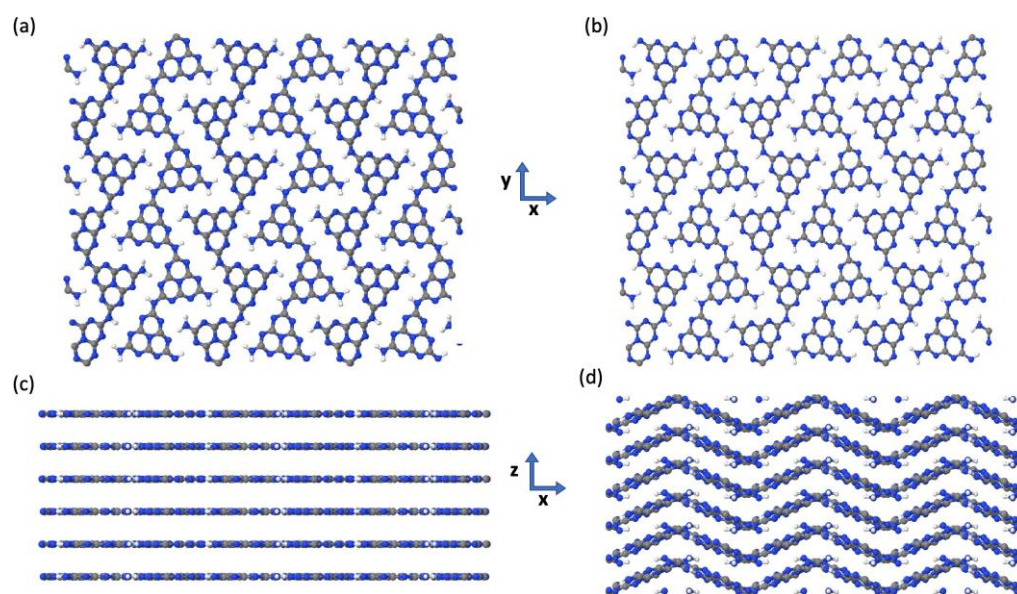


**Figure 2.** Melon structure before ((a,c) panels) [7] and after geometry optimisation ((b,d) panels). Top-view: (a,b) panels; side-view: (c,d) panels, obtained with Jmol program [58].

**Table 1.** Structural parameters of partially condensed melon unit cell. Lattice parameters:  $a, b, c$  [ $v$ ] unit cell vectors;  $\alpha, \beta, \gamma$  [ $^\circ$ ] unit cell angles. Volume of unit cell ( $V$  [ $v^3$ ]), inter-layer distance [ $v$ ], and bending angles before (Fina et al.) and after PBE-D3/621pol optimisation [ $^\circ$ ]. The difference in percentage between the two structures is reported in the last column.

	Fina et al.	PBE-D3	Difference [%]
$a$ [ $v$ ]	16.24	15.18	−6.53
$b$ [ $v$ ]	12.52	12.60	+0.64
$c$ [ $v$ ]	6.52	6.55	+0.46
$\alpha = \beta = \gamma$ [ $^\circ$ ]	90	90	0
$V$ [ $v^3$ ]	1324.90	1253.61	−5.38
Inter-layer distance [ $v$ ]	3.28	3.26	−0.61
Bending angle N77–N86–N130 [ $^\circ$ ]	175.0	150.5	−14.0

The degree of distortion from the planar geometry can be estimated by comparing the bending angle defined as the angle among three in-plane nitrogen atoms univocally identified in Figure S1 of the Supporting Information. The magnitude of this angle changes from  $175^\circ$  in the experimental geometry to  $151^\circ$  in the optimised one.

It is worth noting that the zig-zag layer deformation is also evident at the PBE level, as shown in Figures S1 and S2 of the Supporting Information, and, therefore, cannot be an artifact due to an overestimation of the dispersive interactions between layers due to the D3 correction.

Thus, a notable rumpling of the layers characterises the equilibrium structure of the system calculated at zero Kelvin. The discrepancy between the calculated and experimental structures can be explained by invoking temperature effects. The refined structure, which was obtained at room temperature, could represent the average position of the vibrating lattice structure along the  $z$ -direction, above and below the plane around the equilibrium positions. If at  $T = 0$  K, the interactions between the layers can freeze the structure in one of its lowest energy configurations, as the temperature increases, the kinetic degrees of freedom prevail, the structure vibrates, and the measurements provide the average position of the atoms.

To support the hypothesis of a stabilisation of the structure due to the formation of interactions between layers, we performed a comprehensive search of the charge density

critical points and applied the full machinery of the topological analysis to characterise their nature.

In particular, bond critical points (BCP) were clearly revealed between hydrogen and nitrogen atoms belonging to neighbouring layers. Based on the values of the topological indicators (i.e., Laplacian of the charge density, virial density, ratio between total energy density and charge density), these interactions can be classified as hydrogen bonds, ref. [49] and could be responsible for the rippling of the planes. In addition, similar interactions, H-N, N-N, and C-N in type, were found between intra-layer atoms of neighbouring rows, and these can affect the lattice contraction. As expected, the structure expands due to the increase in temperature, and this explains the difference in volume between the experimental and the computed structures.

As a next step towards the atomic-scale insight into the synthesised sample, a close comparison among the XRD patterns was performed and reported in Figure 3. The XRD analysis computed on the geometry proposed by Fina et al., which is represented by the blue line in Figure 3, shows a good agreement with the pattern measured on our synthesised sample, black line, as both the characteristic peaks, due to the (210) and (002) diffractions, are clearly present. It is worth mentioning that the (002) signal is due to the inter-layer  $\pi$ - $\pi$  stacking, while the (210) is related to in-plane packing of heptazine units. Thus, we can state that at least a partial condensation has been achieved and that our structure corresponds mainly to the melon polymorph with an orthorhombic space group  $P2_12_12$ .

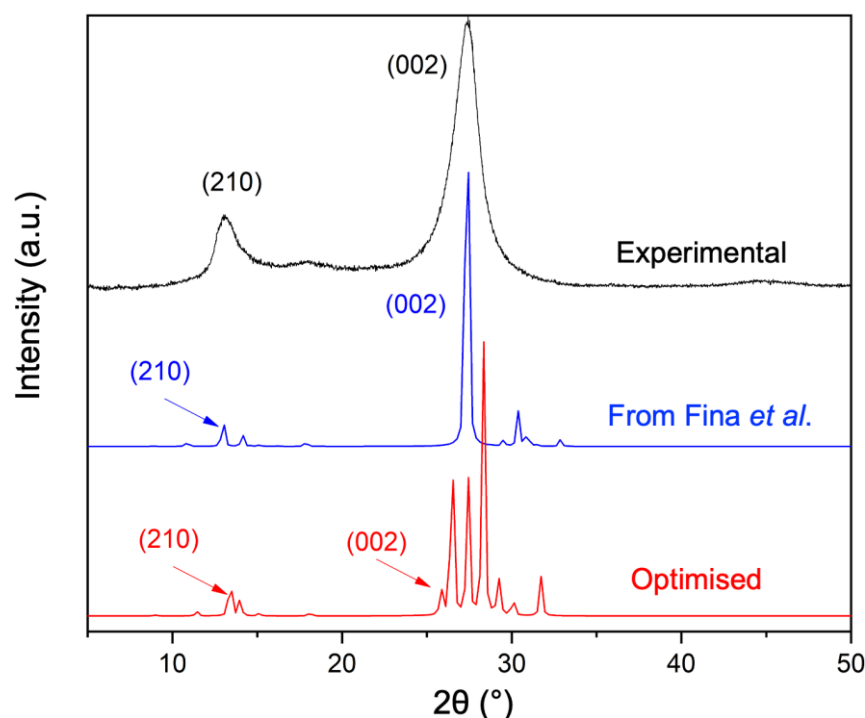


**Figure 3.** XRD diffraction patterns of the experimental structure (black line) compared with the XRD computed diffraction pattern before (Fina et al.) (blue line) and after PBE-D3/621pol optimisation (red line).

Interestingly enough, the XRD pattern of the PBE-D3/621pol optimised structure (red line), shows, besides the features due to the (210) and (002) diffraction planes, additional intense components, within the  $25^\circ < 2\theta < 35^\circ$  range, due to different diffraction lattice planes caused by the rippling of the relaxed geometry.

Concerning the broadening of the experimental features (black line), we assume that it can be explained with an envelope of many XRD features that are reasonably related to different diffraction planes. This makes it possible to hypothesise the occurrence of differently oriented domains inside the synthesised sample. Therefore, for a complete

interpretation of the XRD experimental results, it must be considered that a single model (partially polymerised melon) is not fully representative of the synthesised sample, but a total polymerised model can also be taken into account. According to this, a computational characterisation of a fully polymerised  $g\text{-C}_3\text{N}_4$  structure becomes crucial to accurately reproduce the experimental result.

The most plausible structure for representing the totally polymerised  $g\text{-C}_3\text{N}_4$  has been proposed by Teter and Hamley [35] and belongs to the triclinic lattice, space group 1. In Figure 4, the experimental and PBE-D3/621pol optimised structures are shown for the sake of comparison, and in Table 2, the values of lattice parameters, volume of the reference cell, and the respective percentage variations are detailed. Although less evident with respect to the melon optimised structure, a layer rippling due to inter-/intra-layer interactions is observed on the relaxed structure (fully condensed  $g\text{-C}_3\text{N}_4$  model, Figure 4b,d panels). Moreover, the bending angle between the N6, C21, and N3 atoms undergoes a variation of about 9% instead of 14%, as calculated for the partially condensed melon structure. Finally, a general shortening of the three lattice parameters ( $a$ ,  $b$ , and  $c$ ) that is accompanied by a decrease in volume of about 7% can be noticed.

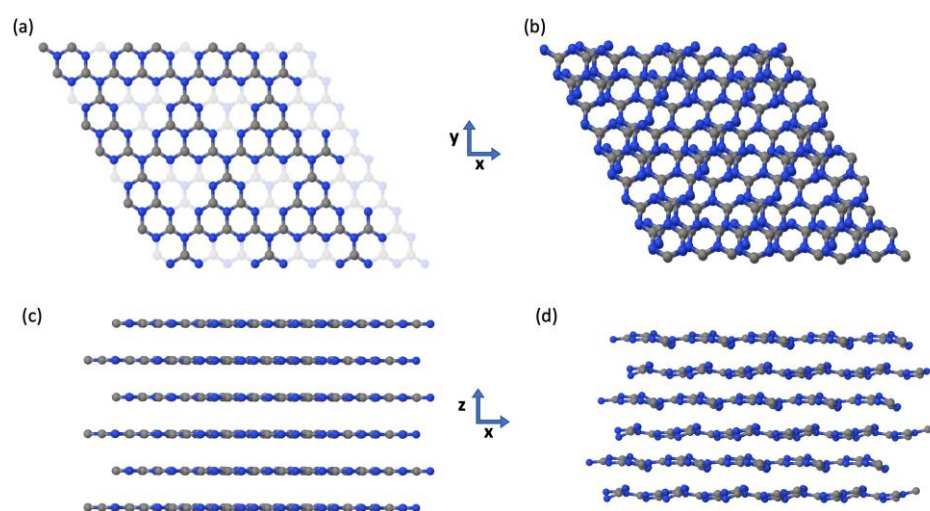


**Figure 4.** Fully condensed  $g\text{-C}_3\text{N}_4$  structure before ((a,c) panels) [35] and after geometry optimisation ((b,d) panels). Top-view: (a,b) panels; side-view: c and d panels, which were obtained with the Jmol program [58].

**Table 2.** Structural parameters of fully condensed  $g\text{-C}_3\text{N}_4$  unit cell. Lattice parameters:  $a$ ,  $b$ ,  $c$  [ $v$ ] unit cell vectors;  $\alpha$ ,  $\beta$ ,  $\gamma$  [ $^\circ$ ] unit cell angles. Volume of unit cell ( $V$  [ $v^3$ ]), inter-layer distance [ $v$ ], and bending angles before (Teter and Hamley [35]) and after PBE-D3/621pol optimisation [ $^\circ$ ]. The difference in percentage between the two structures is reported in the last column.

	Teter and Hamley	PBE-D3	Difference [%]
$a$ [ $v$ ]	7.11	6.99	−1.75
$b$ [ $v$ ]	7.11	6.99	−1.72
$c$ [ $v$ ]	6.49	6.43	−0.99
$\alpha$ [ $^\circ$ ]	90.00	77.58	−13.80
$\beta$ [ $^\circ$ ]	90.00	96.17	+6.86
$\gamma$ [ $^\circ$ ]	120.00	120.01	0.00
$V$ [ $v^3$ ]	284.37	265.47	−6.64
Inter-layer distance [ $v$ ]	3.25	3.12	−4.00
Bending angle N6–C21–N3 [ $^\circ$ ]	180.00	163.90	−8.94

The diffraction patterns that were calculated for the Teter and Hemly geometry (blue line) and for the PBE-D3/621pol relaxed one (red line) are compared with the XRD pattern

measured on our sample, and the agreement is again quite good. The peaks relating to the diffraction planes (002), (210), and (100) are present, although at slightly different  $2\theta$  values with respect to the experimental ones. In agreement with the decreased inter-layer distance of 4%, the position at higher angle values of the computed (002) diffraction angles (blue and red patterns in Figure 5) can be also reasonably explained.

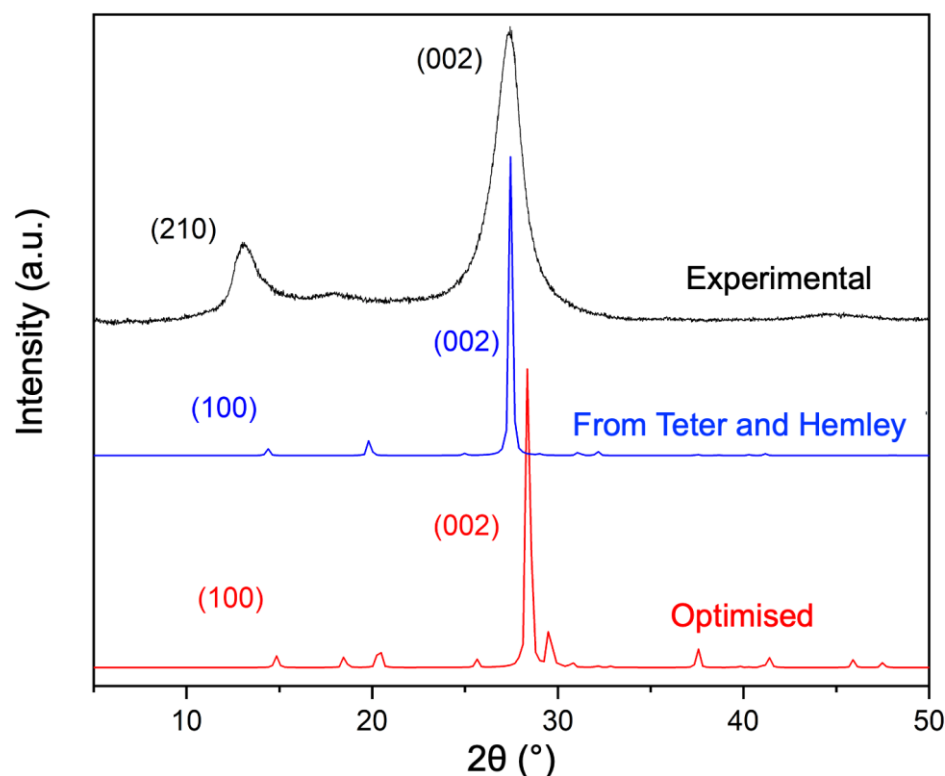


**Figure 5.** XRD diffraction patterns of the experimental structure (black line) compared with the XRD computed diffraction pattern before (Teter and Hemley) (blue line) and after PBE-D3/621pol optimisation (red line).

A more effective comparison between the melon-like and totally polymerised structures discussed so far is shown in Figure S3 Supporting Information.

On the basis of the results discussed so far, we can definitely state that a realistic model, which is able to explain the experimental XRD patterns, implies the combination of different structural motifs including partially (melon-like) and fully polymerised  $g\text{-C}_3\text{N}_4$  structures, as further shown in the following discussion, in agreement with Changbin Im et al. [22].

This result can find an explanation by considering the reaction equilibria along the slow pathway from melamine to fully polymerised  $\text{C}_3\text{N}_4$ . Indeed, the semi-closed reaction environment causes the formation of different volatile compounds including ammonia, which can stabilise several structures with a different polymerisation degree, including the melon-like structure, the fully polymerised  $\text{C}_3\text{N}_4$ , etc., with small differences in thermochemical stability, as confirmed by Changbin Im et al. [22]. (See reaction scheme in Figure S4 in Supporting Information). It is known that low temperatures and high  $p_{\text{NH}_3}$  favour the formation of less condensed melon-string structures, whereas high temperatures and low  $p_{\text{NH}_3}$  lead to more condensed  $g\text{-C}_3\text{N}_4$  systems. Since these limited cases are not representative of the real situation inside the reaction environment, we expect that the obtained material consists of a mixture of less and more condensed structures [22].

#### 4.2. Morphology by SEM and AFM Microscopies

The morphology of the polymerised sample that is obtained from melamine, according to the previously described method, is SEM and AFM imaged in Figure 6.

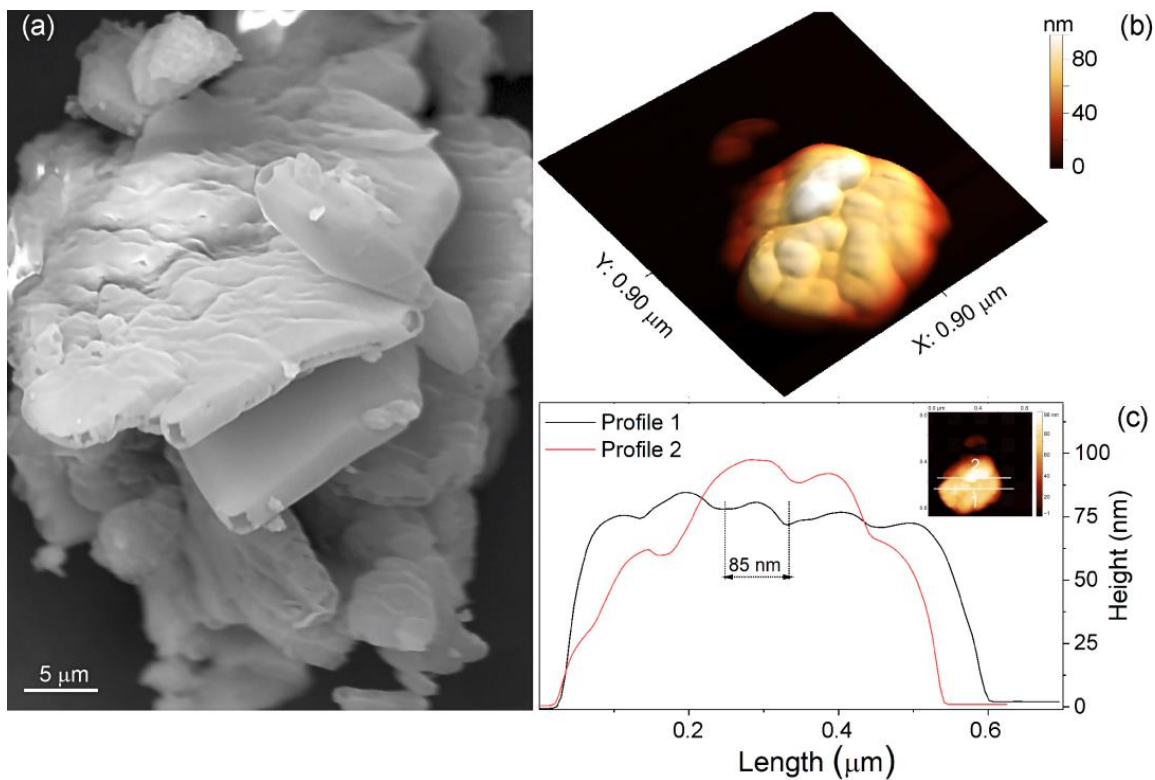


**Figure 6.** (a) SEM image, (b) 3D AFM image, and (c) AFM height profiles along two lines selected in the inset image, which is already shown in (b).

From the SEM image (Figure 6a), a highly heterogeneous material, due to the several chemical processes occurring during the thermal treatment [59], including the decompositions and release of volatile compounds, has been obtained. In particular, complex aggregates of differently elongated rhombohedrons, besides lamellar and hollow structures, which are 5–15 μm in size, can be observed at the adopted resolution.

The high level of aggregation, together with the large size of the lamellar structures, in particular, can be explained with sintering effects due to slow synthesis steps, in agreement with the low specific surface area (see Paragraph 4.1.1).

In Figure 6b, the surface of a portion of g-C<sub>3</sub>N<sub>4</sub> is 3D-AFM imaged on a flat freshly cleaved mica support that again confirms the formation of sintered structures, which are well adhering to each other and consist of large aggregates, as observed from the SEM image (Figure 6a).

Moreover, in Figure 6c, two height profiles along two directions on the inset image are shown. From the observed black and red profiles, the sizes of aggregated polymerised C-N nanoparticles can be estimated in the range of several tens of nanometres. Notice that the high degree of aggregation prevents us from evaluating the size of the single nanoparticles, or of the different domains as obtained from XRD analysis.

#### 4.3. Optical and Electronic Properties Determined via UV-Vis Spectroscopy and DFT Calculations

The optical properties, as well as the electronic structure of the obtained specimen, have been investigated by means of UV-Vis spectroscopy and compared with DFT calculations.

In Figure 7a, the UV-visible spectrum is shown, together with the computed Tauc's plots for indirect (Figure 7b, red dotted line) and direct (Figure 7c, red dotted line) band gap estimations.

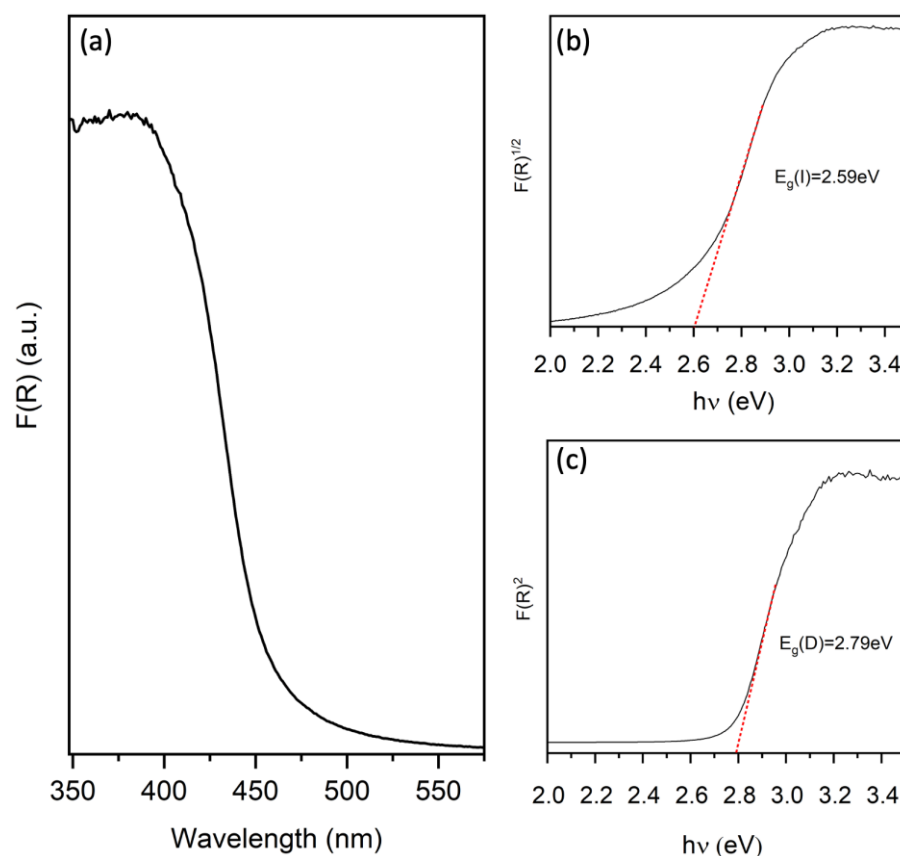


**Figure 7.** UV-vis spectra of g-C<sub>3</sub>N<sub>4</sub> (a); the computed Tauc's plots for indirect (b) and direct (c) band gap estimation.

From Figure 7a, the typical optical absorption edge of the polymerised carbon nitride system, due to the transition from HOMO N<sup>3-</sup> 2p<sub>x,z</sub> antibonding orbitals to the LUMO N<sup>3-</sup> 2p<sub>z</sub> and C<sup>4+</sup> 2p<sub>x,z</sub> lowest-energy orbitals (vide infra), has been observed, and the nitrogen and carbon p<sub>z</sub> orbitals are available as oxidation and reduction sites for O<sub>2</sub> and H<sub>2</sub> evolution reactions, respectively [21].

Furthermore, a remarkable red shift towards longer wavelengths, with respect to melamine (Figure S5 in Supporting Information), can be detected as a result of the high polymerisation degree of our sample. This causes more delocalised  $\pi$ -electrons in the network, either inside the layers or along the stacking direction where the  $\pi$ -orbitals overlap [60]. In particular, from the evaluation of the optical band gap, the extrapolated onset, which is estimated via the Tauc's plots, gives an indirect band gap value of 2.59 eV and a direct band gap value of 2.79 eV (Figure 7b,c, respectively). In the case of melamine, an indirect band gap of 4.71 eV and a direct band gap of 4.84 eV were obtained (Figure S3). Notice that the indirect band gap value of melamine is in agreement with that shown by Liu et al. (4.76 eV) [4]. The results are also consistent with those obtained via the theoretical calculations (vide infra). As a matter of fact, even if many studies have been focused on the investigations of the optical properties of g-C<sub>3</sub>N<sub>4</sub>, identifying the nature of band gap, whether it is direct or indirect, is not always straightforward. Therefore, for a deep understanding of the electronic properties of the material, an accurate description of the electronic band structures of both the partially and totally polymerised systems becomes crucial.

From the band structures shown in Figures 8a and 9a, the semiconductor behaviour of melon and fully condensed g-C<sub>3</sub>N<sub>4</sub> systems, respectively, can be highlighted. In particular, an indirect transition between the Z point at the top of valence band and the  $\Gamma$  point at the bottom of the virtual/conduction band of 2.36 eV and a direct transition from  $\Gamma$  (valence band) to  $\Gamma$  (conduction band) of 2.40 eV were computed for the partially condensed melon

(Figure 8a). These results are in good agreement with the experimental estimation obtained from the Tauc's plots (Figure 7b,c), and with a substantial amount of data reported in the literature [2,3,55,56,60–63], thus establishing that bulk structures show lower band gap than their few-layer or monolayer counterparts, which is expected to enhance the light-harvesting.

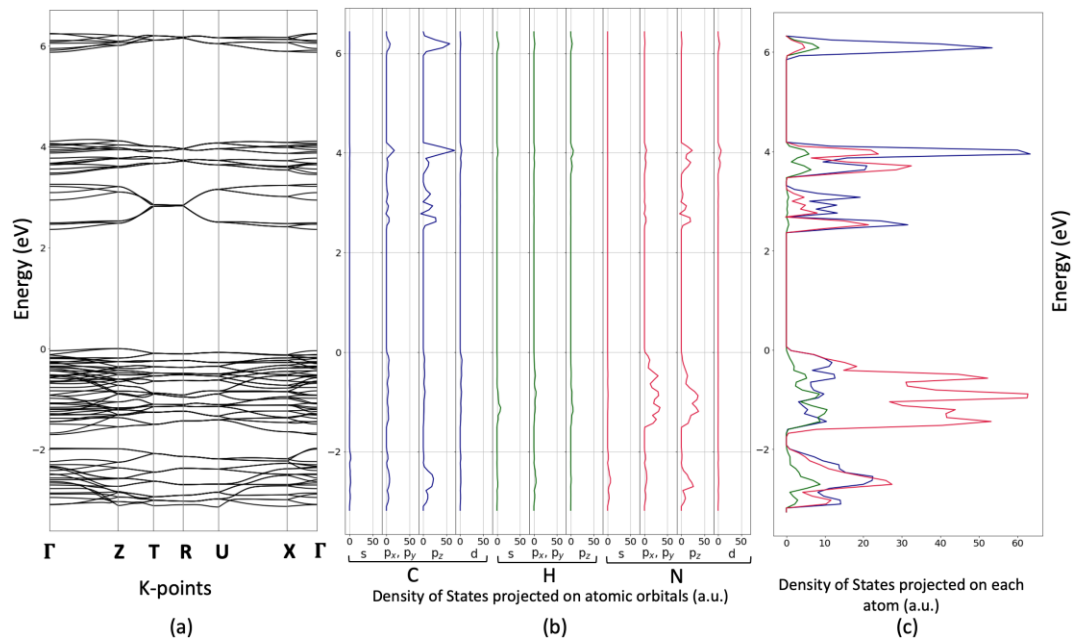


**Figure 8.** Band structure of partially polymerised (melon) system (a); projected density of states (PDOS) on the atomic orbitals (b); projected density of states (PDOS) on each atom (c). (Red lines for nitrogen, blue lines for carbon, green lines for hydrogen).

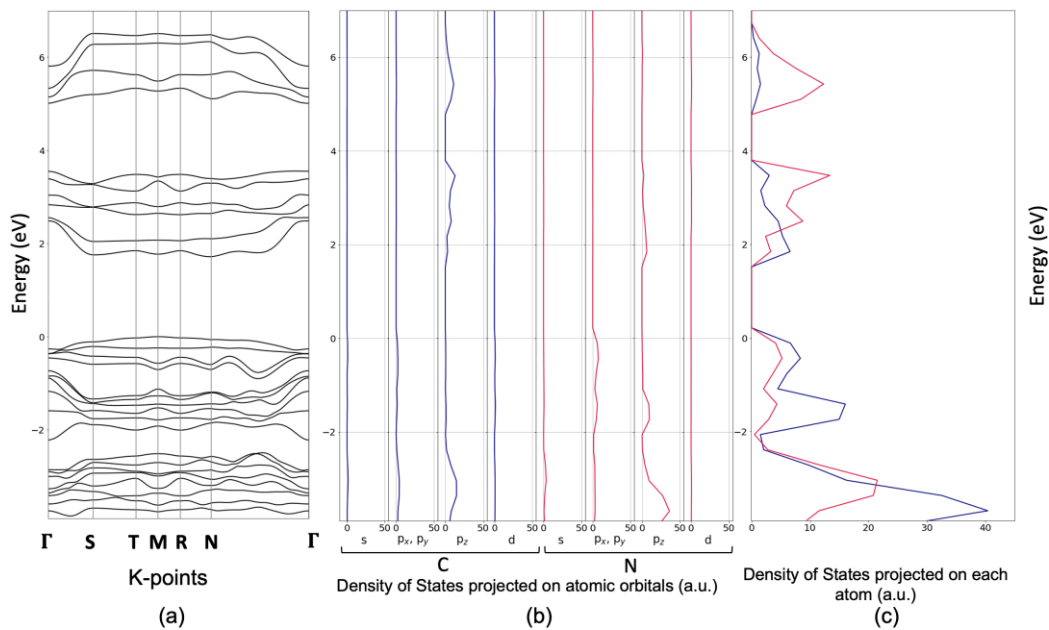


**Figure 9.** Band structure of fully polymerised  $g\text{-C}_3\text{N}_4$  with the selected k-points:  $\Gamma$  (0,0,0), S (0,1/2,0), T (0,1/2,1/2), M (1/4,1/2,1/2), R (1/2,1/2,1/2), and N (3/4,1/2,1/4) (a); projected density of states (PDOS) on the atomic orbitals (b); projected density of states (PDOS) on each atom (c). (Red lines for nitrogen and blue lines for carbon atoms).

Concerning the totally condensed  $g\text{-C}_3\text{N}_4$ , an indirect transition from the N (3/4,1/2,1/4) to the M (1/4, 1/2, 1/2) point of 1.72 eV and a direct transition in the  $\Gamma$  point of 2.75 eV were computed. On the basis of these results, it becomes apparent that the optical properties of our material are better explained by the melon system, given that the computed energy gap is closer to the experimentally estimated one. However, the presence of some totally condensed  $g\text{-C}_3\text{N}_4$  domains within the melon framework could not be excluded. Indeed, either the computed XRD or, mostly, the computed vibrational modes (vide infra), are in agreement with the experimental results, if a coexistence of both structures is taken into account.

Furthermore, the density of states that are projected on both the atomic orbitals and atoms (PDOS) of melon (Figure 8b,c panels, respectively) and of fully condensed  $g\text{-C}_3\text{N}_4$  (Figure 9b,c panels, respectively) has been computed.

By comparing the panel a and b in Figure 8, it becomes apparent that the main contribution to the valence band of melon is mainly due to the  $p_z$  orbitals of nitrogen atoms, while the conduction band consists predominantly of carbon  $p_z$  orbitals, in agreement with Wang et al. [14]. This is further evident from the analysis of the projections on each atomic orbital in Figure 8c, in which the contribution of nitrogen (red lines) and carbon (blue lines) atoms to the valence and conduction band, respectively, are clearly remarkable. As expected, the hydrogen atoms (green line) have a negligible role in the PDOSs projection, even if their contribution in hydrogen bonding interactions between layers and rows is confirmed via the topological analysis of the electron density and supported by FTIR spectra (vide infra).

Concerning the valence and conduction band character, similar considerations can be extended to the total condensed system, except for the absence of hydrogen atoms together with functional end groups such as  $\text{-NH}$  (Figure 9b,c panel). Namely, the majority contribution to the valence band is given by nitrogen  $p_{xy}$  and  $p_z$  orbitals, while the conduction band comes mainly from carbon  $p_z$  orbitals.

#### 4.4. Surface Vibrational Properties Determined via FTIR

FTIR experimental (black line) and computed spectra of partially condensed melon (blue line) and fully condensed  $g\text{-C}_3\text{N}_4$  (red line), together with the experimental spectrum of pristine melamine (grey line), as reference, have been shown in Figure 10.

The wide absorption band in the 3000–3500  $\text{cm}^{-1}$  range of the experimental spectrum can be assigned to the stretching modes of  $\text{NH}/\text{NH}_2$  terminal groups of a melon-like structure [4,6,54–56,61,64–67], while the broadening is explained with H-bonding interactions [53,55]. This assignment is confirmed by the presence of the same features on the pristine melamine spectrum (grey line in Figure 10) [65]. From a close examination of the computed spectrum of melon, the main components inside the experimental convolution band can be identified as a combination of symmetric and asymmetric stretching modes of N-H and  $\text{NH}_2$  functional groups. Notice that due to the absence of  $\text{NH}/\text{NH}_2$  terminal groups in the fully condensed  $g\text{-C}_3\text{N}_4$ , no spectral features are observed in the 3000–3500  $\text{cm}^{-1}$  range, as expected.

Moving to the 1200–1750  $\text{cm}^{-1}$  region (I and II in Figure 10), the typical vibrational modes of C-N heterocycles are found, as also confirmed via the theoretical computation [62]. In particular, the absorptions at 1636  $\text{cm}^{-1}$ , 1558  $\text{cm}^{-1}$  and 1455  $\text{cm}^{-1}$ , 1407  $\text{cm}^{-1}$  (region I), which have already been observed in the pristine melamine sample (grey line in Figure 10), are related to the stretching vibrational modes of C=N and C-N moieties, respectively, within the heterocycles [56,61,64]. By considering the main features of the melon computed spectrum (blue line in region I), the contribution due to the  $\text{-NH}$  and  $\text{-NH}_2$  terminal groups cannot be excluded. Indeed, the feature at 1413  $\text{cm}^{-1}$  can be assigned to the bending mode of the C-NH-C units.

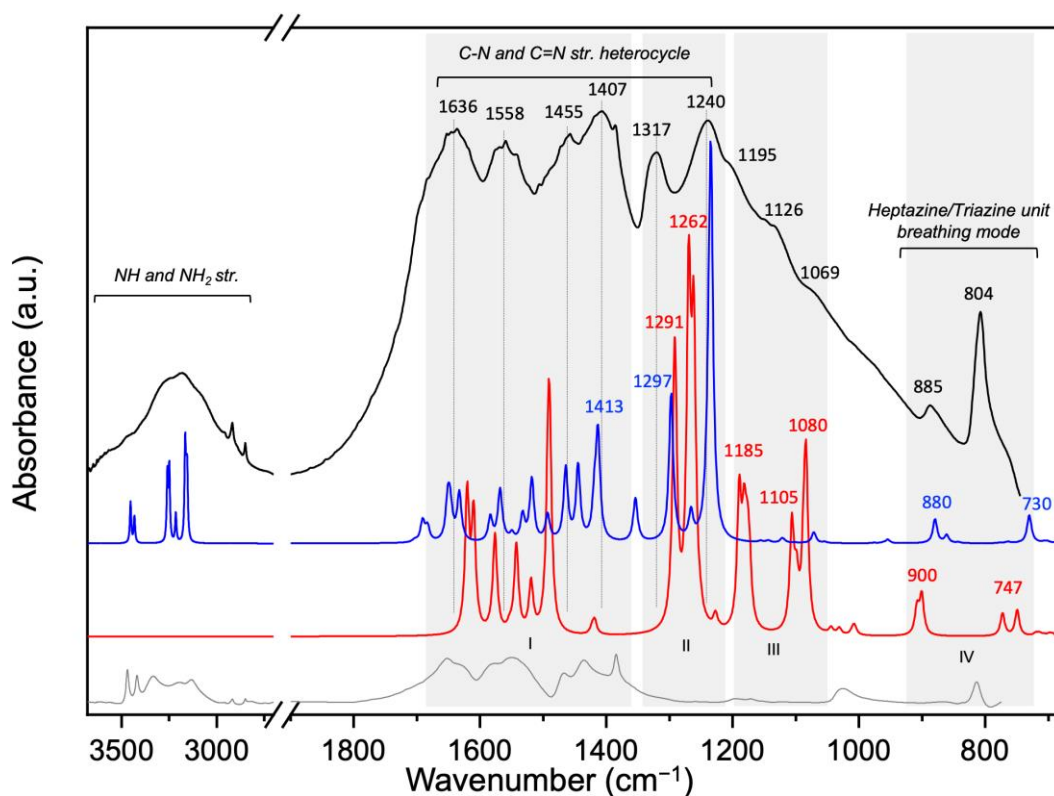
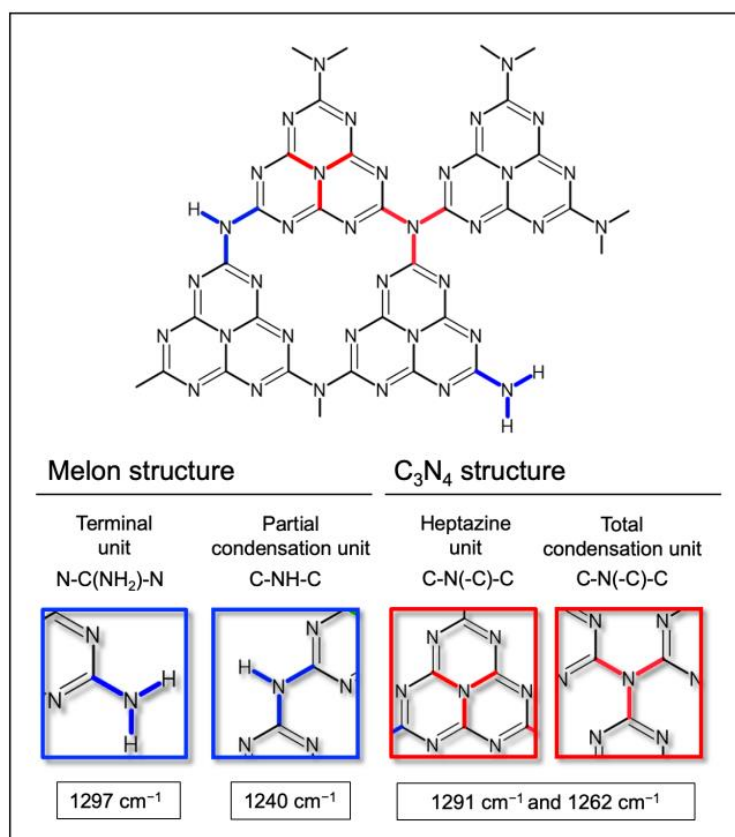


**Figure 10.** FTIR experimental spectra of our sample (black line) and melamine precursor (grey line); computed IR spectra of partially condensed melon (blue line) and fully condensed  $g\text{-C}_3\text{N}_4$  (red line). The main regions of the spectra are highlighted by grey rectangles and labelled with Roman numbers from I to IV.

From the comparison of the experimental FTIR spectra of pristine melamine and our sample (grey and black experimental lines, respectively, in Figure 10), it becomes apparent that the two main absorptions at  $1317\text{ cm}^{-1}$  and  $1240\text{ cm}^{-1}$  (region II), which have quite similar intensity, are absent in the precursor, thus confirming that these features are related to partial (blue line) and/or total (red lines) condensed units. Currently, on the basis of the literature data, the  $1317\text{ cm}^{-1}$  and  $1240\text{ cm}^{-1}$  bands are assigned mainly to the stretching mode of both trigonal C-NH-C units, i.e., the partial-condensation model, or bridging C-N(-C)-C units, which is also called the full-condensation model [6,53,55,64,67,68].

In order to make a more precise assignment, we have to consider the partially condensed melon and the fully condensed  $g\text{-C}_3\text{N}_4$  computed spectra, in which two main features at  $1297\text{ cm}^{-1}$  and at  $1240\text{ cm}^{-1}$  (blue line) and at  $1291\text{ cm}^{-1}$  and at  $1262\text{ cm}^{-1}$  (red line) can be observed.

According to our model of melon structure, we hypothesise that the feature at  $1297\text{ cm}^{-1}$ , which shifted downwards with respect to the experimentally observed one at  $1317\text{ cm}^{-1}$ , can be due to combined collective stretching and bending vibrations of the N-C(NH<sub>2</sub>)-N units, also involving the -NH<sub>2</sub> terminal groups, while the  $1240\text{ cm}^{-1}$  band corresponds mostly to the collective modes of the C-NH-C units involving the -NH groups. Notice that the higher intensity of the  $1240\text{ cm}^{-1}$  band with respect to the other components in the  $1200\text{--}1750\text{ cm}^{-1}$  region of the computed spectrum (blue line) is consistent with our adopted model based on a melon-like structure, which is formed by a sequence of a large number of linked heptazine units. Considering the computed spectrum of the totally condensed system (red line), the features at  $1291\text{ cm}^{-1}$  and at  $1262\text{ cm}^{-1}$  are both ascribed to the C-N(-C)-C total condensed units either inside the heptazine units or among connected moieties as described in Scheme 2.



**Scheme 2.** Structural unit models of melon (blue) and  $C_3N_4$  (red) with relative computed vibrational frequencies.

Furthermore, the three shoulders observed at about  $1195\text{ cm}^{-1}$ ,  $1126\text{ cm}^{-1}$ , and  $1069\text{ cm}^{-1}$  inside the complex envelope of the experimental spectrum (Region III in Figure 10) can be related to the  $1185\text{ cm}^{-1}$ , the  $1105\text{ cm}^{-1}$ , and the  $1080\text{ cm}^{-1}$  computed modes of the totally condensed system (red line). From this, it comes out that the shoulders can be assigned to combined vibrations of domains formed by heptazine units and C-N(C)-C condensed moieties, which connect three heptazine units. It is noteworthy that on the melon computed spectrum (blue line), these modes are absent.

Lastly, the sharp peaks at  $885\text{ cm}^{-1}$  and  $804\text{ cm}^{-1}$  on the experimental spectrum (Region IV) have been assigned to the typical in-plane and out-of-plane bending vibrations (breathing modes) of the heptazine/triazine units [4,6,53–56,61,62,64–67]. These features are also found at  $880\text{ cm}^{-1}$  and  $730\text{ cm}^{-1}$  and at  $900\text{ cm}^{-1}$  and  $747\text{ cm}^{-1}$  on the computed spectra of the partially condensed melon (blue line) and fully condensed system (red line), respectively.

It is noteworthy that, moving from the melamine precursor spectrum (grey line) to the other spectra (both computed and experimental ones), the different intensity ratio between the ( $3000\text{--}3500$  and  $1400\text{--}1600\text{ cm}^{-1}$ ) main regions can be justified with a different amount of the terminal units ( $NH_2$ ) with respect to the number of heterocycle rings. Namely, this provides a further explanation of the condensation of triazine units in more complex structures to form a heptazine lattice.

In conclusion, from a detailed analysis of FTIR spectra, significant information on the polymerisation degree of carbon nitride-based systems can be obtained. In particular, features due to NH/ $NH_2$  stretching vibrations, such as wide absorptions in the  $1200\text{--}1750\text{ cm}^{-1}$  range, which are typical of heterocycle C-N/C=N stretching vibrations, together with the sharp peaks in the  $700\text{--}800\text{ cm}^{-1}$  range due to breathing modes of the heptazine rings, are indicative of a complex structure consisting of totally condensed g-

$C_3N_4$  domains embedded in a partially condensed system, i.e., the melon-string structure formed by a network of linked heptazine units [22,60].

## 5. Conclusions

In summary, polymerised carbon nitride systems have been obtained via a facile one-step calcination method by starting from melamine as an affordable precursor.

The structure analysis based on X-ray powder diffraction makes it possible to highlight the typical layered structure of the semiconductor, while the computational study makes it possible to identify a mixture of both the partially and totally polymerised structures, as expected from the adopted experimental synthesis conditions. Moreover, the geometry optimisation and the topological analysis of the charge density at the PBE-D3/621pol level confirm the tendency of the material to maximise the interactions between layers and rows for both the models.

Combined computation and experimental UV-Vis studies of the electronic properties agree that the material has an indirect band gap with energy values of about 2.59 eV (experimental one), while the theoretical ones are 2.36 eV for the partially polymerised structure and 1.72 eV for the totally condensed g- $C_3N_4$ . The experimental band gap value is likely the result of a complex situation in which more and less condensed motifs, including condensed melamine units, small g- $C_3N_4$  condensed domains, etc., are all embedded in a framework of partially condensed strings, which are formed by a network of linked heptazine units, that is, the melon structure.

In addition, a careful analysis of the FTIR features compared to the computed spectra provides significant information on the frequency values of different functional groups and lattice modes on both systems, thus making it possible to highlight the simultaneous presence of domains with different polymerisation levels inside our synthesised specimen.

In future studies, the concept of a mixed system (based on highly condensed g- $C_3N_4$  domains embedded in a less condensed “melon-like” framework) that was developed in this work will be taken into consideration in order either to explore different synthesis and post-synthesis procedures or to design challenging heterostructures, such as  $C_3N_4/C_3N_4$  homojunctions and/or  $C_3N_4$ /semiconductor heterojunctions, which could be effective in several renewable-energy-activated processes.

**Supplementary Materials:** The following supporting information can be downloaded at: <https://www.mdpi.com/article/10.3390/ma16103644/s1>, Table S1: Lattice parameters and energy gap of melon system computed with different functionals: PBE-D3, PBE0-D3 and HSE06-D3; Figure S1: Graphical view of bending angles before ( $175^\circ$ , on the left side) and after optimisation at PBE-D3 ( $150.5^\circ$ , in the centre) and PBE ( $153.9^\circ$ , on the right side) level; Figure S2. Melon structure optimised at PBE level and relative structural parameters; Figure S3. Comparison of XRD patterns: experimental (black), obtained from Fina et al. model before and after optimisation (blue line), obtained from Teter and Hamley model before and after optimisation (red line). Figure S4. Reaction scheme of direct heating of melamine precursor; Figure S5. UV-vis spectra of melamine (a); the computed Tauc's plots for indirect (b) and direct (c) band gap estimation.

**Author Contributions:** The manuscript was written through contributions of all authors. F.C., P.N., S.C. and D.S. wrote and organised the manuscript; F.C. and P.N., performed experiments and characterisations. In particular: P.N. performed the sample preparation; F.C. performed XRD, SEM and AFM analyses; P.N. performed FTIR and UV-Vis analyses; P.N. and S.C. performed computational analysis; D.S., P.N., F.C. and S.C. provided a substantial contribution to the work; D.S. supervised the manuscript. All authors have read and agreed to the published version of the manuscript.

**Funding:** This research received no external funding.

**Institutional Review Board Statement:** Not applicable.

**Informed Consent Statement:** Not applicable.

**Data Availability Statement:** The data presented in this study are available on request from the corresponding author.

**Acknowledgments:** The authors acknowledge support from CH4.0 under MUR (Ministero dell'Università e della Ricerca) for the university program “Dipartimento di Eccellenza 2023–2027”, INSTM Consorzio, and the NIS (Nanostructured Interfaces and Surfaces) Inter-Departmental Center of University of Torino. The authors thank, in particular, Rosangela Santalucia for her support in FTIR experiments.

**Conflicts of Interest:** The authors declare no conflict of interest.

## References

1. Thomas, A.; Fischer, A.; Goettmann, F.; Antonietti, M.; Müller, J.O.; Schlögl, R.; Carlsson, J.M. Graphitic carbon nitride materials: Variation of structure and morphology and their use as metal-free catalysts. *J. Mater. Chem.* **2008**, *18*, 4893–4908. [[CrossRef](#)]
2. Dong, G.; Zhang, Y.; Pan, Q.; Qiu, J. A fantastic graphitic carbon nitride (g-C<sub>3</sub>N<sub>4</sub>) material: Electronic structure, photocatalytic and photoelectronic properties. *J. Photochem. Photobiol. C Photochem. Rev.* **2014**, *20*, 33–50. [[CrossRef](#)]
3. Wang, J.; Hao, D.; Ye, J.; Umezawa, N. Determination of Crystal Structure of Graphitic Carbon Nitride: Ab Initio Evolutionary Search and Experimental Validation. *Chem. Mater.* **2017**, *29*, 2694–2707. [[CrossRef](#)]
4. Liu, N.; Li, T.; Zhao, Z.; Liu, J.; Luo, X.; Yuan, X.; Luo, K.; Luo, K.; He, J.; Yu, D.; et al. From Triazine to Heptazine: Origin of Graphitic Carbon Nitride as a Photocatalyst. *ACS Omega* **2020**, *5*, 12557–12567. [[CrossRef](#)]
5. Wang, Y.; Zhang, Y.; Li, B.; Luo, K.; Shi, K.; Zhang, L.; Li, Y.; Yu, T.; Hu, W.; Xie, C.; et al. Restacked melon as highly-efficient photocatalyst. *Nano Energy* **2020**, *77*, 105124. [[CrossRef](#)]
6. Lotsch, B.V.; Döblinger, M.; Sehnert, J.; Seyfarth, L.; Senker, J.; Oeckler, O.; Schnick, W. Unmasking melon by a complementary approach employing electron diffraction, solid-state NMR spectroscopy, and theoretical calculations—Structural characterization of a carbon nitride polymer. *Chem.-A Eur. J.* **2007**, *13*, 4969–4980. [[CrossRef](#)]
7. Fina, F.; Callear, S.K.; Carins, G.M.; Irvine, J.T.S. Structural investigation of graphitic carbon nitride via XRD and neutron diffraction. *Chem. Mater.* **2015**, *27*, 2612–2618. [[CrossRef](#)]
8. Ismael, M. A review on graphitic carbon nitride (g-C<sub>3</sub>N<sub>4</sub>) based nanocomposites: Synthesis, categories, and their application in photocatalysis. *J. Alloy. Compd.* **2020**, *846*, 156446. [[CrossRef](#)]
9. Safaei, J.; Mohamed, N.A.; Mohamad Noh, M.F.; Soh, M.F.; Ludin, N.A.; Ibrahim, M.A.; Roslam Wan Isahak, W.N.; Mat Teridi, M.A. Graphitic carbon nitride (g-C<sub>3</sub>N<sub>4</sub>) electrodes for energy conversion and storage: A review on photoelectrochemical water splitting, solar cells and supercapacitors. *J. Mater. Chem. A* **2018**, *6*, 22346–22380. [[CrossRef](#)]
10. Wang, A.; Wang, C.; Fu, L.; Wong-Ng, W.; Lan, Y. Recent advances of graphitic carbon nitride-based structures and applications in catalyst, sensing, imaging, and leds. *Nano-Micro Lett.* **2017**, *9*, 1–21. [[CrossRef](#)]
11. Rhimi, B.; Wang, C.; Bahnemann, D.W. Latest progress in g-C<sub>3</sub>N<sub>4</sub> based heterojunctions for hydrogen production via photocatalytic water splitting: A mini review. *J. Phys. Energy* **2020**, *2*, 042003. [[CrossRef](#)]
12. Hayat, A.; Sohail, M.; Ali Shah Syed, J.; Al-Sehemi, A.G.; Mohammed, M.H.; Al-Ghamdi, A.A.; Taha, T.A.; Salem AlSalem, H.; Alenad, A.M.; Amin, M.A.; et al. Recent Advancement of the Current Aspects of g-C<sub>3</sub>N<sub>4</sub> for its Photocatalytic Applications in Sustainable Energy System. *Chem. Rec.* **2022**, *22*, 202100310. [[CrossRef](#)] [[PubMed](#)]
13. Wang, Y.; Wang, X.; Antonietti, M. Polymeric Graphitic Carbon Nitride as a Heterogeneous Organocatalyst: From Photochemistry to Multipurpose Catalysis to Sustainable Chemistry. *Angew. Chem. Int. Ed.* **2012**, *51*, 68–89. [[CrossRef](#)]
14. Wang, X.; Maeda, K.; Thomas, A.; Takanebe, K.; Xin, G.; Carlsson, J.M.; Domen, K.; Antonietti, M. A metal-free polymeric photocatalyst for hydrogen production from water under visible light. *Nat. Mater.* **2009**, *8*, 76–80. [[CrossRef](#)] [[PubMed](#)]
15. Ong, W.-J.; Tan, L.-L.; Ng, Y.H.; Yong, S.-T.; Chai, S.-P. Graphitic Carbon Nitride (g-C<sub>3</sub>N<sub>4</sub>)-Based Photocatalysts for Artificial Photosynthesis and Environmental Remediation: Are We a Step Closer To Achieving Sustainability? *Chem. Rev.* **2016**, *116*, 7159–7329. [[CrossRef](#)]
16. Liu, G.; Wang, T.; Zhang, H.; Meng, X.; Hao, D.; Chang, K.; Li, P.; Kako, T.; Ye, J. Nature-Inspired Environmental “Phosphorylation” Boosts Photocatalytic H<sub>2</sub> Production over Carbon Nitride Nanosheets under Visible-Light Irradiation. *Angew. Chem. (Int. Ed. Engl.)* **2015**, *54*, 13561–13565. [[CrossRef](#)]
17. Bhunia, M.K.; Yamauchi, K.; Takanebe, K. Harvesting solar light with crystalline carbon nitrides for efficient photocatalytic hydrogen evolution. *Angew. Chem. (Int. Ed. Engl.)* **2014**, *53*, 11001–11005. [[CrossRef](#)]
18. Zhang, Y.; Schnepf, Z.; Cao, J.; Ouyang, S.; Li, Y.; Ye, J.; Liu, S. Biopolymer-Activated Graphitic Carbon Nitride towards a Sustainable Photocathode Material. *Sci. Rep.* **2013**, *3*, 2163. [[CrossRef](#)]
19. Merschjann, C.; Tyborski, T.; Orthmann, S.; Yang, F.; Schwarzburg, K.; Lublow, M.; Lux-Steiner, M.C.; Schedel-Niedrig, T. Photophysics of polymeric carbon nitride: An optical quasimonomer. *Phys. Rev. B* **2013**, *87*, 205204. [[CrossRef](#)]
20. Zhang, Y.; Mori, T.; Niu, L.; Ye, J. Non-covalent doping of graphitic carbon nitride polymer with graphene: Controlled electronic structure and enhanced optoelectronic conversion. *Energy Environ. Sci.* **2011**, *4*, 4517–4521. [[CrossRef](#)]
21. Akhundi, A.; Zaker Moshfegh, A.; Habibi-Yangjeh, A.; Sillanpää, M. Simultaneous Dual-Functional Photocatalysis by g-C<sub>3</sub>N<sub>4</sub>-Based Nanostructures. *ACS EST Eng.* **2022**, *2*, 564–585. [[CrossRef](#)]
22. Im, C.; Kirchoff, B.; Krivtsov, I.; Mitoraj, D.; Beranek, R.; Jacob, T. Structure and Optical Properties of Polymeric Carbon Nitrides from Atomistic Simulations. *Chem. Mater.* **2023**, *35*, 1547–1559. [[CrossRef](#)]

23. Suyana, P.; Ganguly, P.; Nair, B.N.; Pillai, S.C.; Hareesh, U.S. Structural and compositional tuning in g-C<sub>3</sub>N<sub>4</sub> based systems for photocatalytic antibiotic degradation. *Chem. Eng. J. Adv.* **2021**, *8*, 100148. [CrossRef]
24. Wen, J.; Xie, J.; Chen, X.; Li, X. A review on g-C<sub>3</sub>N<sub>4</sub>-based photocatalysts. *Appl. Surf. Sci.* **2017**, *391*, 72–123. [CrossRef]
25. Zheng, Y.; Lin, L.; Wang, B.; Wang, X. Graphitic Carbon Nitride Polymers toward Sustainable Photoredox Catalysis. *Angew. Chem.-Int. Ed.* **2015**, *54*, 12868–12884. [CrossRef]
26. Liu, Y.; Huang, X.; Yu, Z.; Yao, L.; Guo, S.; Zhao, W. Environmentally Friendly Non-Metal Solar Photocatalyst C<sub>3</sub>N<sub>4</sub> for Efficient Nitrogen Fixation as Foliar Fertilizer. *ChemistrySelect* **2020**, *5*, 7720–7727. [CrossRef]
27. Dandia, A.; Gupta, S.L.; Saini, P.; Sharma, R.; Meena, S.; Parewa, V. Structure couture and appraisal of catalytic activity of carbon nitride (g-C<sub>3</sub>N<sub>4</sub>) based materials towards sustainability. *Curr. Res. Green Sustain. Chem.* **2020**, *3*, 100039. [CrossRef]
28. Hartley, G.O.; Martsinovich, N. Computational design of graphitic carbon nitride photocatalysts for water splitting. *Faraday Discuss.* **2021**, *227*, 341–358. [CrossRef]
29. Li, Q.; Jiang, J.; Lin, B.; Ding, D.; Xu, H.; Wang, P.; Chen, Y. Understanding the Surface of g-C<sub>3</sub>N<sub>4</sub>, an Experimental Investigation of the Catalytic Active Site on the Interface. *Catal. Lett.* **2019**, *149*, 3296–3303. [CrossRef]
30. Seyfarth, L.; Seyfarth, J.; Lotsch, B.V.; Schnick, W.; Senker, J. Tackling the stacking disorder of melon—Structure elucidation in a semicrystalline material. *Phys. Chem. Chem. Phys.* **2010**, *12*, 2227–2237. [CrossRef]
31. Schwinghammer, K.; Tuffy, B.; Mesch, M.B.; Wirnhier, E.; Martineau, C.; Taulelle, F.; Schnick, W.; Senker, J.; Lotsch, B.V. Triazine-based carbon nitrides for visible-light-driven hydrogen evolution. *Angew. Chem. (Int. Ed. Engl.)* **2013**, *52*, 2435–2439. [CrossRef] [PubMed]
32. Algara-Siller, G.; Severin, N.; Chong, S.Y.; Björkman, T.; Palgrave, R.G.; Laybourn, A.; Antonietti, M.; Khimiyak, Y.Z.; Krasheninikov, A.V.; Rabe, J.P.; et al. Triazine-based graphitic carbon nitride: A two-dimensional semiconductor. *Angew. Chem. (Int. Ed. Engl.)* **2014**, *53*, 7450–7455. [CrossRef] [PubMed]
33. Villalobos, L.F.; Vahdat, M.T.; Dakhchoune, M.; Nadizadeh, Z.; Mensi, M.; Oveisi, E.; Campi, D.; Marzari, N.; Agrawal, K.V. Large-scale synthesis of crystalline g-C<sub>3</sub>N<sub>4</sub> nanosheets and high-temperature H<sub>2</sub> sieving from assembled films. *Sci. Adv.* **2022**, *6*, eaay9851. [CrossRef] [PubMed]
34. Liu, A.Y.; Cohen, M.L. Prediction of New Low Compressibility Solids. *Science* **1989**, *245*, 841–842. [CrossRef]
35. Teter, D.M.; Hemley, R.J. Low-Compressibility Carbon Nitrides. *Science* **1996**, *271*, 53–55. [CrossRef]
36. Erba, A.; Desmarais, J.K.; Casassa, S.; Civalieri, B.; Donà, L.; Bush, I.J.; Searle, V.; Maschio, L.; Daga, L.-E.; Cossard, A.; et al. CRYSTAL23: A Program for Computational Solid State Physics and Chemistry. *J. Chem. Theory Comput.* **2022**. [CrossRef]
37. CRYSTAL—Basis Sets Library. Available online: <https://www.crystal.unito.it/basis-sets.php> (accessed on 24 March 2023).
38. Perdew, J.P.; Burke, K.; Ernzerhof, M. Generalized Gradient Approximation Made Simple [Phys. Rev. Lett. *77*, 3865 (1996)]. *Phys. Rev. Lett.* **1997**, *78*, 1396. [CrossRef]
39. Perdew, J.P.; Ernzerhof, M.; Burke, K. Rationale for mixing exact exchange with density functional approximations. *J. Chem. Phys.* **1996**, *105*, 9982–9985. [CrossRef]
40. Adamo, C.; Barone, V. Toward reliable density functional methods without adjustable parameters: The PBE0 model. *J. Chem. Phys.* **1999**, *110*, 6158–6170. [CrossRef]
41. Krukau, A.V.; Vydrov, O.A.; Izmaylov, A.F.; Scuseria, G.E. Influence of the exchange screening parameter on the performance of screened hybrid functionals. *J. Chem. Phys.* **2006**, *125*, 224106. [CrossRef]
42. Grimme, S.; Antony, J.; Ehrlich, S.; Krieg, H. A consistent and accurate ab initio parametrization of density functional dispersion correction (DFT-D) for the 94 elements H-Pu. *J. Chem. Phys.* **2010**, *132*, 154104. [CrossRef] [PubMed]
43. Dovesi, R.; Saunders, V.; Roetti, C.; Orlando, R.; Zicovich-Wilson, C.M.; Pascale, F.; Civalieri, B.; Doll, V.; Harrison, N.M.; Bush, V.; et al. CRYSTAL23 User's Manual. **2023**. Available online: <https://www.crystal.unito.it/include/manuals/crystal23.pdf> (accessed on 24 March 2023).
44. Shanno, D.F. Conditioning of Quasi-Newton Methods for Function Minimization. *Math. Comput.* **1970**, *24*, 647–656. [CrossRef]
45. Zicovich-Wilson, C.M.; Dovesi, R. On the use of symmetry-adapted crystalline orbitals in SCF-LCAO periodic calculations. II. Implementation of the self-consistent-field scheme and examples. *Int. J. Quantum Chem.* **1998**, *67*, 311–320. [CrossRef]
46. Pascale, F.; Zicovich-Wilson, C.M.; López Gejo, F.; Civalieri, B.; Orlando, R.; Dovesi, R. The calculation of the vibrational frequencies of crystalline compounds and its implementation in the CRYSTAL code. *J. Comput. Chem.* **2004**, *25*, 888–897. [CrossRef]
47. Zicovich-Wilson, C.M.; Pascale, F.; Roetti, C.; Saunders, V.R.; Orlando, R.; Dovesi, R. Calculation of the vibration frequencies of alpha-quartz: The effect of Hamiltonian and basis set. *J. Comput. Chem.* **2004**, *25*, 1873–1881. [CrossRef]
48. Gatti, C.; Casassa, S. TOPOND 14 User's Manual. Available online: <https://www.crystal.unito.it/topond/topond.pdf> (accessed on 24 March 2023).
49. Gatti, C. Chemical bonding in crystals: New directions. *Z. Krist.-Cryst. Mater.* **2005**, *220*, 399–457. [CrossRef]
50. Casassa, S.; Erba, A.; Baima, J.; Orlando, R. Electron density analysis of large (molecular and periodic) systems: A parallel implementation. *J. Comput. Chem.* **2015**, *36*, 1940–1946. [CrossRef]
51. Eugen Schwarz, W.H.; Richard, F. Bader: Atoms in Molecules (A Quantum Theory) Clarendon Press 1990, Oxford. ISBN 019-855-1681, 438 pages. *Ber. Bunsenges. Phys. Chem.* **1991**, *95*, 1308. [CrossRef]
52. Yuan, Y.; Zhang, L.; Xing, J.; Utama, M.I.B.; Lu, X.; Du, K.; Li, Y.; Hu, X.; Wang, S.; Genç, A.; et al. High-yield synthesis and optical properties of g-C<sub>3</sub>N<sub>4</sub>. *Nanoscale* **2015**, *7*, 12343–12350. [CrossRef]

53. Cao, Y.; Wu, W.; Wang, S.; Peng, H.; Hu, X.; Yu, Y. Monolayer g-C<sub>3</sub>N<sub>4</sub> Fluorescent Sensor for Sensitive and Selective Colorimetric Detection of Silver ion from Aqueous Samples. *J. Fluoresc.* **2016**, *26*, 739–744. [[CrossRef](#)]
54. Li, X.; Zhang, J.; Shen, L.; Ma, Y.; Lei, W.; Cui, Q.; Zou, G. Preparation and characterization of graphitic carbon nitride through pyrolysis of melamine. *Appl. Phys. A Mater. Sci. Process.* **2009**, *94*, 387–392. [[CrossRef](#)]
55. Liu, J.; Zhang, T.; Wang, Z.; Dawson, G.; Chen, W. Simple pyrolysis of urea into graphitic carbon nitride with recyclable adsorption and photocatalytic activity. *J. Mater. Chem.* **2011**, *21*, 14398–14401. [[CrossRef](#)]
56. Ma, Y.; Liu, E.; Hu, X.; Tang, C.; Wan, J.; Li, J.; Fan, J. A simple process to prepare few-layer g-C<sub>3</sub>N<sub>4</sub> nanosheets with enhanced photocatalytic activities. *Appl. Surf. Sci.* **2015**, *358*, 246–251. [[CrossRef](#)]
57. Alizadeh, T.; Nayeri, S.; Hamidi, N. Graphitic carbon nitride (g-C<sub>3</sub>N<sub>4</sub>)/graphite nanocomposite as an extraordinarily sensitive sensor for sub-micromolar detection of oxalic acid in biological samples. *RSC Adv.* **2019**, *9*, 13096–13103. [[CrossRef](#)]
58. Jmol: An Open-Source Java Viewer for Chemical Structures in 3D. Available online: <https://jmol.sourceforge.net> (accessed on 24 March 2023).
59. Costa, L.; Camino, G. Thermal behaviour of melamine. *J. Therm. Anal.* **1988**, *34*, 423–429. [[CrossRef](#)]
60. Inoki, H.; Seo, G.; Kanai, K. Synthesis of graphitic carbon nitride under low ammonia partial pressure. *Appl. Surf. Sci.* **2020**, *534*, 147569. [[CrossRef](#)]
61. Martha, S.; Nashim, A.; Parida, K.M. Facile synthesis of highly active g-C<sub>3</sub>N<sub>4</sub> for efficient hydrogen production under visible light. *J. Mater. Chem. A* **2013**, *1*, 7816–7824. [[CrossRef](#)]
62. Yan, S.C.; Li, Z.S.; Zou, Z.G. Photodegradation performance of g-C<sub>3</sub>N<sub>4</sub> fabricated by directly heating melamine. *Langmuir* **2009**, *25*, 10397–10401. [[CrossRef](#)]
63. Wei, W.; Jacob, T. Strong excitonic effects in the optical properties of graphitic carbon nitride g-C<sub>3</sub>N<sub>4</sub> from first principles. *Phys. Rev. B-Condens. Matter Mater. Phys.* **2013**, *87*, 1–7. [[CrossRef](#)]
64. Wu, P.; Wang, J.; Zhao, J.; Guo, L.; Osterloh, F.E. Structure defects in g-C<sub>3</sub>N<sub>4</sub> limit visible light driven hydrogen evolution and photovoltage. *J. Mater. Chem. A* **2014**, *2*, 20338–20344. [[CrossRef](#)]
65. Wang, S.; Li, C.; Wang, T.; Zhang, P.; Li, A.; Gong, J. Controllable synthesis of nanotube-type graphitic C<sub>3</sub>N<sub>4</sub> and their visible-light photocatalytic and fluorescent properties. *J. Mater. Chem. A* **2014**, *2*, 2885–2890. [[CrossRef](#)]
66. Zhao, Y.C.; Yu, D.L.; Zhou, H.W.; Tian, Y.J.; Yanagisawa, O. Turbostratic carbon nitride prepared by pyrolysis of melamine. *J. Mater. Sci.* **2005**, *40*, 2645–2647. [[CrossRef](#)]
67. Qiu, P.; Chen, H.; Xu, C.; Zhou, N.; Jiang, F.; Wang, X.; Fu, Y. Fabrication of an exfoliated graphitic carbon nitride as a highly active visible light photocatalyst. *J. Mater. Chem. A* **2015**, *3*, 24237–24244. [[CrossRef](#)]
68. Mitoraj, D.; Kisch, H. On the Mechanism of Urea-Induced Titania Modification. *Chem.–A Eur. J.* **2010**, *16*, 261–269. [[CrossRef](#)]

**Disclaimer/Publisher’s Note:** The statements, opinions and data contained in all publications are solely those of the individual author(s) and contributor(s) and not of MDPI and/or the editor(s). MDPI and/or the editor(s) disclaim responsibility for any injury to people or property resulting from any ideas, methods, instructions or products referred to in the content.